

**Global Ocean Surface Velocities from Drifters: Mean, Variance, ENSO Response,
and Seasonal Cycle**

Rick Lumpkin¹ and Gregory C. Johnson²
for *Journal of Geophysical Research–Oceans*

Draft 24 September 2012

¹NOAA/Atlantic Oceanographic and Meteorological Laboratory, 4301 Rickenbacker
Causeway, Miami FL 33149 USA

²NOAA/Pacific Marine Environmental Laboratory, 7600 Sand Point Way NE Bldg. 3,
Seattle WA 98115 USA

e-mail: Rick.Lumpkin@noaa.gov

ABSTRACT

Global near-surface currents are calculated from satellite-tracked drogued drifter velocities on a $0.5^\circ \times 0.5^\circ$ latitude-longitude grid using a new methodology. Data used at each grid point lie within a centered bin of set area with a shape defined by the variance ellipse of current fluctuations within that bin. The time mean current, its annual harmonic, semiannual harmonic, correlation with the Southern Oscillation Index (SOI), spatial gradients, and residuals are estimated along with formal error bars for each component. The time mean field resolves the major surface current systems of the world. The magnitude of the variance reveals enhanced eddy kinetic energy in the western boundary current systems, and along the Antarctic Circumpolar Current, as well as three large “eddy deserts”, two in the Pacific and one in the Atlantic. The SOI component is largest in the western and central tropical Pacific, but can also be seen in the Indian Ocean basin. Seasonal variations reveal details such as the gyre-scale shifts in the convergence centers of the subtropical gyres and the seasonal evolution of tropical currents and eddies in the western tropical Pacific Ocean. The results of this study are available as a monthly climatology.

1. Introduction

Knowledge of global near-surface currents is important for a variety of uses including ship routing, search and rescue efforts, biological and chemical studies, and both hindcasts and forecasts of the transport and dispersion of floating material including plastic and oil [c.f., *McCord et al.*, 1999; *Davidson et al.*, 2009; *Yoder et al.*, 1994; *Law et al.*, 2010; *Maximenko et al.*, 2012]. Here we apply a new methodology to derive the global distribution of time-mean near-surface ocean currents, their seasonal cycle, their projection onto the Southern Oscillation Index (ENSO), and the variance of eddy fluctuations from a homogeneous data set of global near-surface current observations from the satellite-tracked drifters of the Global Drifter Program (GDP) [*Niiler*, 2001; *Lumpkin and Pazos*, 2007].

Although previous studies have derived a global mean surface velocity field from GDP drifter observations [c.f., *Maximenko et al.*, 2009], they have suffered from contamination by undiagnosed drogue loss for a significant fraction of the data [*Grodsky et al.*, 2011; *Rio et al.*, 2011]. GDP drifters have a drogue (sea anchor) centered at a depth of 15 m to reduce the downwind slip (motion with respect to the current at 15 m depth) to $\sim 0.1\%$ of the wind speed for winds up to 10 m s^{-1} [*Niiler et al.*, 1995] and follow the water within the mixed layer. When this drogue is lost, the downwind slip increases to $\sim 1\text{--}1.5\%$ of the wind speed [*Pazan and Niiler*, 2001; *Poulain et al.*, 2009; *Lumpkin et al.*, 2012]. A recent reanalysis of drogue presence has removed undrogued data from the GDP data set [*Lumpkin et al.*, 2012]. Here we set out a new method for binning and mapping the data that captures spatial and temporal variations in the data and

produces formal error bars for the mapped velocity components. These results are made available at http://www.aoml.noaa.gov/phod/dac/dac_meanvel.php¹.

2. Data and Methods

This analysis uses quality controlled data from the GDP from 1979 through December 2011, interpolated via kriging to regular 6-hour intervals [*Hansen and Poulain*, 1996]. Velocities every 6 hours are obtained via 12-hour centered differencing of the kriged positions. Recent analyses have found a significant fraction of the velocities in the time period 2002—2009 previously believed to be from drogued drifters were from undrogued drifters; in this study, only data from drogued drifters are used, following results of a manual reevaluation of drogue presence [*Lumpkin et al.*, 2012]. NCEP operational 6-hour winds W are interpolated to the drifter locations and a downwind slip of $7 \times 10^{-4} W$ [*Niiler and Paduan*, 1995] is removed from the remaining drifter velocities. The resulting velocities are lowpassed with a 2-point Butterworth filter with half-power cutoff at five days to remove tidal and near-inertial components of the flow, then decimated to daily values for this analysis. No attempt is made to separate Ekman and geostrophic velocities [e.g., *Lumpkin and Garzoli*, 2005].

Following *Johnson* [2001], zonal and meridional drifter speeds are mapped in elliptical bins centered on a $0.5^\circ \times 0.5^\circ$ longitude-latitude grid, with the ratio of semi-major to semi-minor axis and axis orientation set by the variance ellipse of eddy

¹ Note to referees: this will be done pending publication; in the interim, the climatology is available at ftp://ftp.aoml.noaa.gov/phod/pub/lumpkin/greg/meandrift_world.mat. In this file, U, V, T contain the monthly climatology of currents and drifter-measured SST (dimensions: Lat \times Lon \times 12, 1) with associated error bars (Lat \times Lon \times 12, 2). Ubar (Lat \times Lon \times 11, 1) contains all 11 coefficients for the model fit Az to zonal speed, with associated error bars Ubar(Lat \times Lon \times 11, 2), and Vbar for meridional speed. Up2bar, Vp2bar and UpVpbar are $\langle u'^2 \rangle$, $\langle v'^2 \rangle$ and $\langle u'v' \rangle$, respectively.

fluctuations (residuals with respect to the mapped current within the bin; see below) in the bin. For this study we chose bins with a set area of $\pi \times 2^\circ \text{ lat.} \times 2^\circ \text{ long.}$ Hence the bin area at $\pm 60^\circ$ latitude is half that at the equator, reflecting, albeit only weakly, the reduction of the Rossby radius of deformation at high latitudes [e.g. *Chelton et al.*, 1998], and its influence in reducing ocean current scales at higher latitudes [e.g., *Stammer et al.*, 2007].

Within each bin, the complex vector \mathbf{u} containing observations $u + iv$ of zonal u and meridional v drifter speed can be written $\mathbf{u} = \mathbf{A}\mathbf{z} + \mathbf{u}'$, where \mathbf{u}' are residuals (eddy fluctuations), \mathbf{z} is a vector containing 11 coefficients to be determined, and matrix \mathbf{A} describes the model used to map the large-scale currents:

$$\mathbf{A}_j = [1 \quad SOI_j \quad \sin(2\pi t_j) \quad \cos(2\pi t_j) \quad \sin(4\pi t_j) \quad \cos(4\pi t_j) \quad x_j \quad x_j^2 \quad y_j \quad y_j^2 \quad x_j y_j]. \quad (1)$$

Here the subscript j indicates observation j collected at time t_j (in years). The unity term models the time mean. The term SOI_j is a running five-month average of the Southern Oscillation Index [*Trenberth*, 1984] centered at t_j ; this term models the influence of ENSO, and is especially important near the equator, where drifter observations may be biased towards El Niño-related periods of weak Trade Winds and associated low equatorial divergence [*Johnson*, 2001]. The sinusoidal terms fit annual and semi-annual harmonics [*Johnson*, 2001; *Lumpkin*, 2003]. The final five terms in \mathbf{A}_j capture spatial gradients within the bin [*Bauer et al.*, 1998; *Johnson*, 2001] and are expressed with respect to the non-dimensionalized zonal distance x_j and meridional distance y_j from the bin center, expressed in degrees longitude or latitude divided by 1° .

The model is evaluated iteratively, starting with a circular bin, and calculating the resulting variance ellipses to determine a new ellipsoidal bin and new model coefficients

[c.f., *Johnson*, 2001]. The calculation is iterated a total of five times for each bin to ensure convergence.

The Gauss-Markov estimator for \mathbf{z} in a given bin is

$$\mathbf{z} = \mathbf{R}_z \mathbf{A}^T (\mathbf{A} \mathbf{R}_z \mathbf{A}^T + \mathbf{R}_n)^{-1} \mathbf{u}, \quad (2)$$

[c.f., *Wunsch*, 1996; *Lumpkin*, 2003], where \mathbf{R}_z is the *a priori* (calculated before solving for \mathbf{z}) covariance matrix of the unknown coefficients in \mathbf{z} and \mathbf{R}_n is the variance structure of the eddy noise \mathbf{u} . For this study each of the diagonal elements of \mathbf{R}_x are assumed to be equal to the squared range of \mathbf{u} and off-diagonal elements were set to zero. In principle prior knowledge could guide the values of the terms in \mathbf{R}_n ; our choice to set them all equal assumes that any term in (1) could potentially account for the observed variance of \mathbf{u} in each bin. Elements of \mathbf{R}_n are chosen to be

$$R_n(\tau) = [\text{std}(u)^2 + i \text{std}(v)^2] \cos(\pi\tau / 2T_d) \exp[-(\pi\tau / 2\sqrt{2} T_d)^2] \quad (3)$$

following *Lumpkin* [2003], with $T_d = 10.33$ days, consistent with an integral eddy time scale of five days. This choice assigns degrees of freedom to the observations with the assumption that observations less than five days apart are not fully independent [*Lumpkin*, 2003]. The *a posteriori* error covariance matrix is

$$\mathbf{P}_z = \mathbf{R}_z - \mathbf{R}_z \mathbf{A}^T (\mathbf{A} \mathbf{R}_z \mathbf{A}^T + \mathbf{R}_n)^{-1} \mathbf{A} \mathbf{R}_z \quad (4)$$

[c.f., *Wunsch*, 1996]. The square roots of the diagonal terms in \mathbf{P}_z are the formal error bars for the coefficients in \mathbf{z} ; for example, $[\mathbf{P}_z(1,1)]^{0.5}$ is the error for time-mean \mathbf{u} at the bin center. The total squared error for the mapped speed $\mathbf{A}\mathbf{z}$ is $\mathbf{A}\mathbf{P}_z\mathbf{A}^T$. This quantity can, for example, be used to derive error bars on seasonal or monthly mean values. The magnitudes of the coefficients \mathbf{z} and the residuals \mathbf{u} are compared against the prior values (square roots of the diagonal terms in \mathbf{R}_z and \mathbf{R}_n , respectively) in each bin. The

solution in a bin is rejected if $|z|$ exceeds the prior value in \mathbf{R}_z or if more than 40% of the residuals exceeds the prior value in \mathbf{R}_n .

The number of daily observations within each bin is highly inhomogeneous (Fig. 1), being a function of deployment locations and the subsequent advection pathways, including regions of divergence and convergence that impact drifter residence times. Regions of poor data coverage (< 50 drifter days per square degree) are located in the southernmost Southern Ocean, the southeast Pacific Ocean west of Chile, the Southern Ocean south of Australia, the southwest Pacific immediately north of New Zealand, the western equatorial Indian Ocean, the central equatorial Atlantic Ocean, the easternmost Angola Basin, and the Java Sea (much of which is shallower than 15 m). The data are also not homogeneous in time: the earliest deployments (in 1979) were conducted solely in the tropical Pacific Ocean as part of the Tropical Ocean Global Atmosphere study [Niiler, 2001]. Sustained deployments began in the North Atlantic in 1989 [Fratantoni, 2001], the South Atlantic in 1993, the Indian Ocean in 1994, and the Tropical Atlantic in 1997 [Lumpkin and Garzoli, 2005]. From 1993–2002, the array averaged 500–700 drifters at any given time; it was increased to its current size of ~1250 drifters in late 2005 and has been subsequently sustained at approximately this size [Lumpkin and Pazos, 2007].

3. Results

We start with a presentation of the mean speed and streamlines as well as variance ellipses. We then discuss the regression of surface currents onto the SOI. Following that, we present the global seasonal cycle of the surface currents. As examples of the details

visible in the climatology, we discuss the seasonal cycle of surface currents in the western tropical Pacific Ocean and the surface divergence fields of the equatorial interior ocean basins. We conclude with a comparison to an oft-used surface current product.

3.1. Mean fields

Unsmoothed mean current speeds (to indicate current magnitudes) with streamlines calculated from spatially smoothed velocities (to indicate current directions as well as qualitatively, the surface divergence field) clearly illustrate the prominent large-scale currents (Fig. 2) such as the western boundary currents, their extensions, the equatorial current systems, and parts of the Antarctic Circumpolar Current (ACC). The global histogram of mean speed (not shown) peaks at $4.5\text{--}6\text{ cm s}^{-1}$, with 87% of the bins having a mean speed $< 25\text{ cm s}^{-1}$ and 98% $< 50\text{ cm s}^{-1}$.

3.1.1 Prominent currents

The structure of the Antarctic Circumpolar Current (ACC) is resolved as strong jets associated with the Southern Ocean fronts, surrounded by regions of relatively weak flow [Orsi *et al.*, 1995; Falco and Zambianci, 2011]. The ACC bifurcates east of the Drake Passage (Fig. 2), with a significant portion flowing north in the western Atlantic as the Malvinas Current, perhaps the equivalent of the western boundary for this otherwise zonally unbounded current [e.g. Baker, 1982]. After meeting the southward-flowing Brazil Current at the Brazil/Malvinas Confluence, the southern Confluence jet continues eastward across the South Atlantic and enters the southern Indian Ocean basin. Paralleling this to the south, the southern fronts of the ACC enter the Indian Ocean sector

and slowly migrates southward as they flow eastward through the Indian and Pacific sectors [e.g., Orsi *et al.*, 1995; Falco and Zambianci, 2011]. The ACC is narrower and in some areas up to 10 cm s^{-1} weaker than in previous mean current fields calculated from drifters prior to the recent drogue presence reassessment [Lumpkin *et al.*, 2012]. The ACC is not resolved in the southeast Pacific sector due to the scarcity of drogued data in this region.

In the northern and equatorial Indian Ocean, with its strong seasonal cycle [e.g. Schott and McCreary, 2001], discussed below, the time-mean surface currents (Fig. 2) are dominated by the northward-flowing Somali western boundary current and eastward equatorial Wyrki Jet. In the Indian Ocean, the westward-flowing South Equatorial Current (SEC) at $24\text{--}6.5^\circ\text{S}$ is shifted further south than in the other oceans, with a maximum speed of $20\text{--}24 \text{ cm s}^{-1}$ at 12°S . The SEC is fed in part by the Indonesian Throughflow [Gordon *et al.*, 1997]. It bifurcates near 16°S upon reaching Madagascar, with the northern branch heading westward to Africa and then turning northward to join the East Africa Current [e.g., Swallow *et al.*, 1988]. The fate of the southern branch of the East Madagascar Current when it reaches the southern end of Madagascar is less clear [e.g., Lutjeharms, 2007], but in the mean drifter climatology it appears to form a jet extending west-southwest from the southern tip of Madagascar to 28°S , 40°W . This jet then splits, with one branch flowing southward to join the Agulhas return current and the other flowing westward to join with the southward-flowing Mozambique Current to feed the Agulhas Current. The Agulhas has time-mean speeds of $60\text{--}150 \text{ cm s}^{-1}$, with the greatest speeds found from 32.5°S , 29°E to 34.5°S , 25.5°E . The Agulhas retroflects south of Africa, at $20\text{--}23^\circ\text{E}$ in the mean, to feed the eastward-flowing Agulhas Return

Current which exhibits prominent meanders as it flows eastward to $\sim 45^\circ\text{E}$ and then east-southeastward to eventually merge with the ACC. On the east side of the Indian Ocean, the Leeuwin Current flows south along the west coast of Australia [Feng *et al.*, 2003], with a speed of $20\text{--}35\text{ cm s}^{-1}$ in the latitude band $24\text{--}26.5^\circ\text{S}$, but it appears in the mean to be interrupted by an anti-cyclonic feature centered at $\sim 29^\circ\text{S}$, 111°E ; northward currents on the west side of this feature oppose the Leeuwin and reduce its strength. South of 30°S the Leeuwin exceeds 100 cm s^{-1} in several bins. The Leeuwin Current wraps around the southwest corner of Australia and continues eastward along Australia's south coast.

In the North Pacific, the Alaskan Stream [Reed, 1984] is apparent in the mean surface velocity from the drifter data (Fig. 2) just south of Alaska and the Aleutian Island chain, petering out by about 170°E after it leaves its effective western boundary, near the dateline, where the island chain curves back to the northwest. The southward-flowing East Kamchatka and Oyashio, the western boundary currents of the subpolar gyre, are less prominent than the northward-flowing Kuroshio of the subtropical gyre, as is their eastward-flowing extension [e.g. Qu *et al.*, 2001] which slows to eastward speeds $<10\text{ cm s}^{-1}$ by 170°W .

The equatorial Pacific currents are prominent in the drifter velocities (Fig. 2), with the westward flowing North Equatorial Current (NEC) at $9\text{--}24^\circ\text{N}$ with a peak speed of 20 cm/s at 11°N when averaged in the zonal band $150^\circ\text{E}\text{--}140^\circ\text{W}$. The NEC extends from about 120°W to the Philippines, where it bifurcates to feed the northward-flowing Kuroshio and the southward flowing Mindanao Current [e.g. Toole *et al.*, 1990]. The Costa Rica Dome stands out as a small isolated anti-cyclonic circulation centered near

212 9°N, 95°W [*Fiedler, 2002*]. To the northwest, a region of anti-cyclonic circulation at 12–
 213 15°N, 105–95°W may be the rectified signature of the wind-generated anti-cyclonic
 214 Tehuantepec and Papagayo eddies which are generated in this region from October to
 215 July [*Palacios and Bograd, 2005*]; when the mean is recalculated using only August and
 216 September data (not shown), the eastward flow on the northern half of this region is not
 217 present. The North Equatorial Countercurrent (NECC) extends all the way across the
 218 Pacific [e.g. *Johnson et al., 2002*]. In the Pacific the SEC is strongest at very low
 219 latitudes, with a narrow, $\sim 45 \text{ cm s}^{-1}$ (averaged from 180–100°W) branch at 2°N and a
 220 larger branch of maximum speed 30–35 cm s^{-1} centered at 4°S at 140–110°W which
 221 gradually shifts northward as it flows west, reaching 2°S by the dateline. These branches
 222 are separated by eastward surface flow at the equator in the central to eastern Pacific (the
 223 shoaled equatorial undercurrent) [*Johnson et al., 2002*], although this feature is not
 224 readily apparent in the smoothed streamlines. The SEC is also strong along about 15°S
 225 from the dateline into the Coral Sea, where it bifurcates at the east coast of Australia,
 226 with part heading north towards the equator via the Solomon Sea and the New Guinea
 227 Coastal Current and another portion feeding the southward flowing East Australia
 228 Current [e.g., *Ganachaud et al., 2008*] which has a peak speed of 90 cm s^{-1} at 30.5°S,
 229 153.5°E.

230 In the subpolar North Atlantic Ocean, the 30–35 cm s^{-1} East Greenland Current
 231 rounds Cape Farewell to become the west Greenland current with peak speeds of 45–50
 232 cm s^{-1} , and then the 15–30 cm s^{-1} Labrador Current, before meeting the Gulf Stream
 233 extension near Newfoundland [e.g., *Higginson et al., 2011*]. The northward-flowing
 234 Norwegian Atlantic Current is also prominent in the drifter data [e.g., *Poulin et al.,*

1996]. In the southwestern tropical Atlantic, a portion of the North Brazil Current [Garzoli *et al.*, 2004; Lumpkin and Garzoli, 2005] enters the Caribbean to form the 30–50 cm s⁻¹ Caribbean Current, which passes north of a clearly defined Columbia-Panama gyre in the southern Columbia Basin [c.f. Richardson, 2005]. The Caribbean Current feeds into the Loop Current in the Gulf of Mexico, which in turn joins the Gulf Stream flowing north to Cape Hatteras, where it turns eastward to feed the North Atlantic Current [e.g., Schmitz and McCartney, 1993]. In the time-mean the Gulf Stream is 70–80 cm s⁻¹, with speeds exceeding 90 cm s⁻¹ in the Florida Current and at its separation from the coast near Cape Hatteras. The tropical Atlantic circulation is dominated by a zonally elongated clockwise gyre consisting of the westward northern and central branches of the SEC, the northwestward North Brazil Current (NBC) and its southeastward retroflection, and the eastward NECC and Guinea Current [Lumpkin and Garzoli, 2005]. Very large time-mean speeds of 80–140 cm s⁻¹ are found in the NBC, with the largest speeds located at 4–7°N, 54–50°W immediately before the NBC splits into the southeastward Retroflection and the westward Guyana Current. Upwelling and cross-equatorial flow of surface waters evident in the mean surface drifter climatology (Fig. 2) play a role in the warm return flow of the Atlantic Meridional Overturning Circulation [e.g., Roemmich, 1981].

In the South Atlantic, the southern SEC bifurcates against the South American coast at 14–14.5°S to form the north-northeastward NBC and the south-southwestward Brazil Current. The Brazil Current meets the north-northeastward Malvinas Current at 37°S, 54°W in the time-mean. The Brazil-Malvinas Confluence is a complex, energetic region [e.g. Provost *et al.*, 1992, Lumpkin and Garzoli, 2011]; in the mean drifter climatology the Malvinas Current has speeds of 30–50 cm s⁻¹ against the South American

shelf, with comparable speeds in the southward Brazil/Malvinas Confluence jet which extends south to about 45°S. The eastward flow emerging from the Confluence region is strongest at 48°S, associated with the Subpolar Front, with a secondary jet at 40°S associated with the Subtropical Front [Orsi *et al.*, 1995].

3.1.2 Interior gyres, convergence, and divergence.

Global streamlines converge in the centers of the subtropical gyres, associated with the convergent subtropical fronts (Fig. 2). These fronts terminate in so-called garbage patches in the both hemispheres of the eastern Pacific and the eastern South Indian oceans [Maximenko *et al.*, 2012]. In the Atlantic the convergences are centered further to the west [e.g., Law *et al.*, 2011]. In contrast, streamlines diverge from the subpolar gyres of the North Pacific and North Atlantic. Subpolar divergence south of the ACC, where deep water is upwelled [e.g., Sloyan and Rintoul, 2001], is not resolved by the drifters.

Divergence from the equatorial Pacific and Atlantic is also extremely prominent (Fig. 2), and is associated with the cold tongues of upwelled water from below [e.g. Johnson *et al.*, 2001; Grodsky and Carton, 2002]. However, in the equatorial Indian Ocean, acceleration of the flow across the equator is consistent with weaker horizontal divergence (see Section 3.3) that is not as visually apparent as in the equatorial Pacific and Atlantic. In fact, there is a net southward surface flow observed at the equator, closing a mean cell of subducted water in the Southern Hemisphere and upwelled water in the North [Schott *et al.*, 2004]. Divergence is apparent near 8°S in the western tropical

Indian Ocean, where the winds bring the thermocline close to the surface [e.g., *Hermes and Reason*, 2008], as well as in the Costa Rica Dome near 9°N, 90°W [*Fiedler*, 2002].

Streamlines also clearly diverge from the west coasts of North and South America and Africa (apart from the latitude band of the NECC, Fig. 2), where the equatorward-flowing eastern boundary currents are associated with coastal upwelling [e.g. *Bograd et al.*, 2009; *Colas et al.*, 2012; *Hutchings et al.*, 2009; *Nyckær and Van Camp*, 1994]. In contrast, the streamlines do not indicate divergence along the Australian west coast, where the poleward-flowing Leeuwin Current carries warm water southward, and the winds and circulation inhibit upwelling [*Feng et al.*, 2003].

3.2 Variance

The mean speed of eddy fluctuations with respect to the model fit (i.e., fluctuations with respect to the time-mean, seasonal, and SOI-related variations, equal to the square root of twice the eddy kinetic energy) shows large geographic variations (Fig. 3). These results are comparable to those from satellite altimetry [e.g., *Ducet et al.*, 2000], except that the surface drifter analysis can be carried to the equator as geostrophy need not be assumed. Maximum eddy speeds exceeding 70 cm s⁻¹ are found in the Somali Current region; values > 60 cm s⁻¹ are also found in the Gulf Stream and Agulhas Retroflection, and > 50 cm s⁻¹ also in the Loop Current, Florida Current, the Pacific NECC and northern SEC at 115–130°W (presumably associated with energetic Tropical Instability Waves), Kuroshio Current, Brazil/Malvinas Confluence, Agulhas Return Current, North Brazil Current Retroflection, Mozambique Channel, and the East Australian Current. Enhanced eddy energy is also seen along the path of the ACC, west

of the Hawaiian Islands, in the Pacific Subtropical Countercurrents, and along much of the NECCs of the Atlantic and Pacific basins.

In contrast, “eddy deserts” with time-mean eddy speeds $< 10 \text{ cm s}^{-1}$ dominate three large regions: the subtropical South Atlantic, the subpolar North Pacific, and the southeastern South Pacific ($\sim 110\text{--}85^\circ\text{W}$ from $40\text{--}10^\circ\text{S}$, and extending west to 170°W in the band $45\text{--}35^\circ\text{S}$). Much smaller eddy deserts are found in the central subtropical North Atlantic, west and south of New Zealand and south of the merged Agulhas Return Current and ACC immediately south of Kerguelen Island.

The variance ellipses for these eddy fluctuations (Fig. 3) tend to align with most of the major currents such as the Gulf Stream and Kuroshio, although this tendency is less apparent in the East Australia and the Agulhas Return currents. Near the coasts, the ellipses tend to align with the coastlines. In the ocean interiors they are generally more circular, except at low latitudes, particularly in the Pacific and Indian equatorial bands, where they are zonally elongated.

3.3 Southern Oscillation Index (SOI) and surface currents

Current speeds and directions from the regression against the SOI (Fig. 4, plotted for $\text{SOI} = -1$, corresponding to a moderate El Niño) contain the anticipated eastward (and slightly equatorially convergent) surge of surface currents in the Equatorial Pacific [e.g. *Johnson et al.*, 2000]. Eastward values of $10\text{--}20 \text{ cm s}^{-1}$ are seen in the equatorial Pacific ($2^\circ\text{S}\text{--}3^\circ\text{N}$) from 160°E to nearly 160°W , and along $155\text{--}110^\circ\text{W}$ from $2\text{--}3^\circ\text{N}$. A weaker response mirroring the $2\text{--}3^\circ\text{N}$ response is seen just south of the equator in the eastern tropical Pacific. East of 145°W , the response on the equator is not statistically

significantly different from zero due to the scarcity of observations (Fig. 1). In the western tropical South Pacific there is another patch of anomalous westward flow associated with an El Niño-related shift in the South Pacific Convergence Zone [e.g., *Cai et al.*, 2012]. Curiously, the response in the Tehuantepec and Papagayo eddy region 12–15°N, 105–95°W suggests a weakening of the anti-cyclonic recirculation even though more frequent and stronger anti-cyclonic eddies are thought to be generated there during El Niños [*Palacios and Bograd*, 2005].

In the Indian Ocean, El Niño-related westward speeds of $\sim 4\text{--}8\text{ cm s}^{-1}$ can be found in a band stretching west-northwestward across the basin from $\sim 12^\circ\text{S}$, 100°E to $\sim 1^\circ\text{N}$, 50°E , generally increasing toward the west. There is another patch of westward flow just north of the equator south of India and Sri Lanka. The large spatial extent and coherent directions in these features suggest they may be robust. Other less spatially coherent patterns include a slowing of the surface currents in the Gulf Stream during El Niños, eastward flow in the deep eastern Bering Sea, and anomalous westward flow in the Mediterranean Sea. There are isolated patches of response in other areas, but nothing aside from the patterns already discussed stands out as spatially coherent.

3.4. Seasonal variations

Monthly mean ocean currents for climatological February, August, May, and November (Figs. 5–6) illustrate the seasonal cycle of global surface currents. For example, the eastward Wyrtki jet in the equatorial Indian Ocean is prominent in May ($\sim 50\text{ cm s}^{-1}$) and November ($\sim 70\text{ cm s}^{-1}$) while being absent in August and reversed in February [e.g. *Nagura and McPhaden*, 2010]. Likewise the Somali Current is completely

spun-up in August during the Southwest Monsoon, but reversed in February near the end of the Northeast Monsoon [e.g. *Schott et al.*, 1990]. The Bay of Bengal shows a strong seasonal cycle as well, with current directions reversing completely [e.g., *Shenoi et al.*, 1999]. Interior flow across the equator is largely southward in August, and northward in February, with seasonally reversing surface winds driving a shallow “cross-equatorial roll” with subsurface flow opposite the surface flow [e.g. *Schott et al.*, 2002]. Further to the south, the surface expression of the South Equatorial Current is substantially weaker in August than in other seasons.

The seasonality of the NECC is clearly seen in the Pacific and Atlantic basins, revealing for example an intense Atlantic NECC emerging from the North Brazil Current Retroflection in August while neither exists in May [e.g., *Lumpkin and Garzoli*, 2005]. The Pacific NECC is quite strong in August and November, but much weaker in February and May [e.g. *Johnson et al.*, 2002]. The South Equatorial Countercurrent in the western Pacific Ocean at 11–8°S is clearly seen in February (and also in December, January and March, not shown) while being absent in other months [*Chen and Qiu*, 2004].

The gyre-scale circulations (Figs. 5–6, streamlines) also exhibit seasonal migrations, which are no doubt associated with seasonal wind shifts [vis., *Risien and Chelton*, 2008]. For example, the centers of the northern hemisphere subtropical gyres shift to the south in February and to the north in August. In the North Pacific Ocean there is a dramatic shift in the latitude of the interior recirculation gyre, from ~20°N in February to ~40°N in August. This seasonal migration may have a significant modulating impact on the convergence of floating material in the “garbage patch” of the

North Pacific, compared to calculations based on time-mean Lagrangian displacement statistics [e.g., *Maximeko et al.*, 2012] in which these shifts would spuriously increase the effective time-mean lateral diffusivity.

3.4.1 Tropical west Pacific surface currents

Many fine-scale details of the surface circulation are difficult to see when plotted at the global scale, but are resolved by the drifter observations in the climatology presented here. For example, in the western Pacific (Fig. 7) the southward-flowing Mindanao Current can be seen to split immediately north of the northeastern tip of the Celebes year-round, with the westward branch entering the Celebes Sea, and the eastward branch feeding the NECC; the cyclonic Mindanao Eddy is located between the Mindanao Current and NECC throughout the year [c.f., *Arruda and Nof*, 2003]. In Boreal winter, the strongly zonal NECC separates into its main branch running along $\sim 5^\circ\text{N}$ and a secondary branch flowing ESE along the northwestern New Guinea coast (Fig. 7). This branch reverses through Boreal spring, and by August the WNW New Guinea Coastal Current (NGCC) has surfaced. At the confluence of the Mindanao Current's eastward branch and the NGCC, a narrow northeastward-flowing jet develops, the eastern side of which recirculates to form the Halmahera Eddy [c.f., *Arruda and Nof*, 2003] which is not present in Boreal winter but is clearly visible in Boreal summer through fall. This eddy is thought to play a significant role in modulating exchange between the Pacific and Indian basins through the Indonesian Throughflow [*Qu et al.*, 1999].

3.4.2. Interior equatorial surface divergence

The seasonal divergence in the equatorial interior of the three ocean basins (Fig. 8) contrast strongly. Equatorial divergence in the Indian Ocean peaks in August with the relaxation of the Wyrtki Jet; the flow is strongly convergent in November through January. An off-equatorial divergence is evident in the South Indian Ocean, centered near 8°S in December–April, and closer to 5°S in May–August. This feature may be associated with the thermocline ridge near that latitude in the South Indian Ocean [e.g., *Hermes and Reason*, 2008]. In contrast, equatorial divergence is present year-round in the central Pacific and Atlantic basins [e.g., *Johnson et al.*, 2001; *Grodsky and Carton*, 2002], although the magnitude displays a seasonal modulation in both basins with stronger divergence in Boreal spring vs. Boreal fall (mirroring the development of the cold tongue in the eastern regions of these basins). Off-equatorial convergence is seen throughout the year in the central Pacific south of the equator, but is more seasonally modulated to the north with a convergence maximum at 4–5°N in May–June. In the central Atlantic, convergent maxima are seen at 4–8° N during May–August, and at 6–4°S during June–September. These patterns of equatorial divergence and off-equatorial convergence are associated with the shallow tropical overturning cells in these basins [e.g. *Perez et al.*, 2010].

4. Summary and Discussion

We use a global set of drogued drifter velocity measurements to map the time-mean, seasonal and Southern Oscillation Index-related components of near-surface currents at high resolution. Our approach combines aspects of three previous mapping efforts [*Bauer et al.*, 1998; *Johnson*, 2001; *Lumpkin*, 2003] to address spatial and

temporal variations in the data and to produce formal error bars for the various components (mean, seasonal cycle, SOI regression) of the currents. Our analysis also takes advantage of data set corrections from a recent reevaluation of drogue presence [Lumpkin *et al.*, 2012], one result of which is significantly reduced speeds for currents such as the ACC. However, it is possible that downwind (and down-wave) slip, which has not been directly measured for drogued drifters at wind speeds $>10 \text{ m s}^{-1}$ [Niiler *et al.*, 1995], may exceed the linear slip removed in the recent data set update by Lumpkin *et al.* [2012], and as such there may still be downwind bias in regions of strong winds.

Assuming a mean density of 1025 kg m^{-3} , the global distribution of total kinetic energy (Fig. 9d) is equivalent to $8.8 \times 10^{17} \text{ J}$ of energy in the upper 30 m, in all bins with more than 12 drifter days per square degree (for reference, the global total variable kinetic energy of the full-depth ocean is estimated at $3.8 \times 10^{18} \text{ J}$ [Wunsch, 1998]). Mean currents contribute a substantial fraction to the total kinetic energy (Fig. 9a) where one would expect: in the western boundary currents and their extensions, in the North Equatorial currents and the North Equatorial countercurrents of the Atlantic and Pacific oceans, and in segments of the Antarctic Circumpolar Current. These are all locations where the total kinetic energy is high (Fig. 9d), and – except for the equatorial currents and regions of the ACC – where there is topographic confinement. However, the mean currents also constitute a substantial fraction of the total kinetic energy in the South Equatorial currents of all three oceans as well as in the interior of the subpolar North Pacific gyre, all eddy desert regions (with the exception of the Indian Ocean SEC) where the total kinetic energy is relatively low. Globally, the mean currents contribute $2.9 \times 10^{17} \text{ J}$ of kinetic energy in the upper 30 m, 33% of the total estimated KE.

441 The seasonal contribution (Fig. 9c) to the total kinetic energy (Fig. 9d) is 20–40%
442 in the Pacific and Atlantic North Equatorial countercurrents. It is substantial throughout
443 much of the Indian Ocean north of about 10°S, with maxima of 50–70% at 0–5°N, 55–
444 70°E. Another location of strong seasonal contribution is the eastern tropical South
445 Atlantic Ocean, just west of Africa: it contributes 20–30% of the total KE throughout the
446 Angola Basin, and 40–70% against the African coast. Seasonal variations represent a
447 global total of 1.1×10^{17} J of kinetic energy in the upper 30 m, 13% of the total KE.

448 The fractional contribution of SOI-related variations (not shown) is generally
449 small, exceeding 10% only in the vicinity of the equator from 165°E to 165°W. It
450 represents a global total of 7.8×10^{15} J of kinetic energy in the upper 30 m, 1% of the
451 total.

452 The eddy contribution (Fig. 9b) to the total kinetic energy (Fig. 10d) dominates
453 much of the ocean, especially the interior of the subtropical gyres and the subpolar North
454 Atlantic Gyre. The fraction of the total kinetic energy accounted for by eddies exceeds
455 50% in 71% of the bins. However, in much of this area the total kinetic energy is small.
456 EKE dominates in the well-known eddy regions such as the Gulf Stream and Kuroshio
457 recirculation gyres, Agulhas and North Brazil Current ring pathways, and the
458 Brazil/Malvinas Confluence. Eddies also make a large contribution between the North
459 Equatorial currents and the various branches of the South Equatorial currents, where
460 tropical instability waves [e.g. *Chelton et al.*, 1999] are energetic. The eddy deserts of
461 the eastern North Pacific, eastern South Atlantic, and eastern South Pacific each have
462 portions where mean currents are dominant, but also portions where the eddies are

dominant, with low total energy levels throughout. The EKE represents a total of 4.6×10^{17} J of kinetic energy in the upper 30 m, 53% of the total KE.

The climatology of time-mean and seasonal currents described here is available at http://www.aoml.noaa.gov/phod/dac/dac_meanvel.php. This climatology can be used for purposes such as model validation and product evaluation. For example, there are large and spatially coherent differences (Fig. 10a) between the mean velocity in the drifter climatology and the January 1993–December 2003 mean velocity from the $1/3^\circ$ unfiltered satellite-derived Ocean Surface Current Analysis Real-time (OSCAR) product [Bonjean and Lagerloef, 2002] including geostrophic, Ekman, and buoyancy components. While inter-annual variations may play a role in some of the discrepancies, the drifter climatology is faster by up to $20\text{--}25\text{ cm s}^{-1}$ in the Gulf Stream and Kuroshio currents, and up to 35 cm s^{-1} faster in segments of the ACC and Agulhas Return Current. Along the northern branch of the South Equatorial Current at $1\text{--}3^\circ\text{N}$ in the Pacific, the drifter climatology is $20\text{--}50\text{ cm s}^{-1}$ faster to the west than in the OSCAR product; on the equator in the Atlantic it is $20\text{--}35\text{ cm s}^{-1}$ faster to the west (Fig. 10). These dramatic differences may be due both to smoothing and difficulties in calculating the near-equatorial quasi-geostrophic flow for OSCAR.

Differences between this new drifter-derived climatology and products giving time-mean geostrophic speed (such as the CNES-CLS09 MDT product [Rio *et al.* 2011], Fig. 10b) can be used to infer the ageostrophic component of drifter motion. Although it extends beyond the scope of this study, it would be interesting to remove the ageostrophic motion, recalculate the distribution of variance about the time-mean speeds, and compare the results to eddy kinetic energy from altimetry [c.f., Fratantoni, 2001].

486 Because the drifter climatology gives total near-surface currents, it can also be used to
487 improve our estimates of wind stress and turbulent heat fluxes, which depend on the
488 relative speed of the wind over the moving ocean surface [*Fairall et al.*, 2003]. Ocean
489 currents have been demonstrated to affect the wind stress field and its curl and divergence
490 [*Kelly et al.*, 2001; *Risien and Chelton*, 2008].

491

492

Acknowledgments. NOAA Research and the NOAA Climate Program Office funded this work. RL received additional support from the Atlantic Oceanographic and Meteorological Laboratory. Conversations and input from Chris Meinen, Carlisle Thacker, and Kathleen Dohan helped improve the original manuscript. The drifter data were collected and made freely available by the Global Drifter Program (<http://www.aoml.noaa.gov/envids/gld/index.php>). OSCAR data are available at <http://www.oscar.noaa.gov>. PMEL publication 3902.

References

- Arruda, W. Z. and D. Nof (2003), The Mindanao and Halmahera Eddies—Twin Eddies Induced by Nonlinearities, *J. Phys. Oceanogr.*, *33*, 2815–2830.
- Baker, D. J. (1982), A note on Sverdrup balance in the Southern Ocean, *J. Mar. Res.*, *40*, (Suppl.), S21–S26.
- Bauer, S., M. S. Swenson, A. Griffa, A. J. Mariano, and K. Owens (1998), Eddy–mean flow decomposition and eddy-diffusivity estimates in the tropical Pacific Ocean. 1. Methodology, *J. Geophys. Res.*, *103*(C13), 30,855–30,871, doi:10.1029/1998JC900009.
- Bograd, S. J., I. Schroeder, N. Sarkar, X. Qiu, W. J. Sydeman, and F. B. Schwing (2009), Phenology of coastal upwelling in the California Current, *Geophys. Res. Lett.*, *36*, L01602, doi:10.1029/2008GL035933.
- Bonjean, F. and G. S. Lagerloef (2002). Diagnostic Model and Analysis of the Surface Currents in the Tropical Pacific Ocean, *J. Phys. Oceanogr.*, *32*, 2938–2954.
- Cai, W., and co-authors (2012), More extreme swings of the South Pacific convergence zone due to greenhouse warming, *Nature*, *488*, 365–369, doi:10.1038/nature11358.
- Chelton, D. B., R. A. deSzoek, M. G. Schlax, K. El Naggar, and N. Siwertz (1998), Geographical variability of the first baroclinic Rossby radius of deformation, *J. Phys. Oceanogr.*, *28*, 433–460. doi: [http://dx.doi.org/10.1175/1520-0485\(1998\)028<0433:GVOTFB>2.0.CO;2](http://dx.doi.org/10.1175/1520-0485(1998)028<0433:GVOTFB>2.0.CO;2).
- Chelton, D. B., F. J. Wentz, C. L. Gentemann, R. A. de Szoek, and M. G. Schlax (2000), Satellite microwave SST observations of transequatorial tropical instability waves, *Geophys. Res. Lett.*, *27*, 1239–1242, doi:10.1029/1999GL011047.

522 Chen, S., and B. Qiu (2004), Seasonal variability of the South Equatorial Countercurrent,
523 *J. Geophys. Res.*, *109*, C08003, doi:10.1029/2003JC002243.

524 Colas, F., J. C. McWilliams, X. Capet and J. Kurian (2012), Heat balance and eddies in
525 the Peru-Chile current system, *Climate Dynamics*, *39*, 509–529, doi: 10.1007/s00382-
526 011-1170-6.

527 Davidson, F. J. M., A. Allen, G. B. Brassington, Ø. Breivik, P. Daniel, M. Kamachi, S.
528 Sato, B. King, F. Lefevre, M. Sutton, and H. Kaneko (2009), Applications of GODAE
529 ocean current forecasts to search and rescue and ship routing, *Oceanogr.* *22*(3):176–
530 181, <http://dx.doi.org/10.5670/oceanog.2009.76>.

531 Ducet, N., P.-Y. Le Traon, and G. Reverdin (2000), Global high-resolution mapping of
532 ocean circulation from TOPEX/Poseidon and ERS-1 and -2, *J. Geophys. Res.*, *105*,
533 19,477–19,498, doi:10.1029/2000JC900063.

534 Fairall, C.W., Bradley, E.F., Hare, J.E., Grachev, A.A., and Edson, J.B. (2003), Bulk
535 parameterization of air-sea fluxes: Updates and verification for the COARE
536 algorithm, *J. Climate*, *16*, 571–591. Falco, P., and E. Zambianchi (2011), Near-surface
537 structure of the Antarctic Circumpolar Current derived from World Ocean Circulation
538 Experiment drifter data, *J. Geophys. Res.*, *116*, C05003, doi:10.1029/2010JC006349.

539 Feng, M., G. Meyers, A. Pearce, and S. Wijffels (2003), Annual and interannual
540 variations of the Leeuwin Current at 32°S, *J. Geophys. Res.*, *108*, 3355,
541 doi:10.1029/2002JC001763.

542 Fiedler, P. C. (2002), The annual cycle and biological effects of the Costa Rica Dome.
543 *Deep-Sea Res. II*, *49*, 321–338, doi: 10.1016/S0967-0637(01)00057-7.

544 Fratantoni, D. M. (2001), North Atlantic surface circulation during the 1990's observed

545 with satellite-tracked drifters, *J. Geophys. Res.-Oceans*, *106* (C10), 22,067–22,093.

546 Ganachaud, A., L. Gourdeau, and W. Kessler (2008), Bifurcation of the subtropical South
547 Equatorial Current against New Caledonia in December 2004 from a hydrographic
548 inverse box model, *J. Phys. Oceanogr.*, *38*, 2072–2084, doi:10.1175/2008JPO3901.1.

549 Garzoli, S. L., A. Ffield, W. E. Johns, and Q. Yao (2004), North Brazil Current
550 retroflection and transports, *J. Geophys. Res.*, *109*, C01013,
551 doi:10.1029/2003JC001775.

552 Gordon, A. L., S. Ma, D. B. Olson, P. Hacker, A. Ffield, L. D. Talley, D. Wilson, and M.
553 Baringer (1997), Advection and diffusion of Indonesian Throughflow Water within
554 the Indian Ocean South Equatorial Current, *Geophys. Res. Lett.*, *24*, 2573–2576,
555 doi:10.1029/97GL01061.

556 Grodsky, S. A. and J. A. Carton (2002), Surface drifter pathways originating in the
557 equatorial Atlantic cold tongue, *Geophys. Res. Lett.*, *29*, 2147,
558 doi:10.1029/2002GL015788.

559 Grodsky, S. A., R. Lumpkin, and J. A. Carton (2011), Spurious trends in global surface
560 drifter currents, *Geophys. Res. Lett.*, *38*, L10606, doi:10.1029/2011GL047393.

561 Hansen, D., and P.-M. Poulain (1996), Quality control and interpolations of WOCE-
562 TOGA drifter data, *J. Atmos. Oceanic Technol.*, *13*, 900–909.

563 Hermes, J. C., and C. J. C. Reason (2008), Annual cycle of the South Indian Ocean
564 (Seychelles-Chagos) thermocline ridge in a regional ocean model, *J. Geophys. Res.*,
565 *113*, C04035, doi:10.1029/2007JC004363.

566 Higginson, S., K. R. Thompson, J. Huang, M. Véronneau, and D. G. Wright (2011), The
567 mean surface circulation of the North Atlantic subpolar gyre: A comparison of

568 estimates derived from new gravity and oceanographic measurements, *J. Geophys.*
 569 *Res.*, *116*, C08016, doi:10.1029/2010JC006877.
 570 Hutchings, L., and co-authors (2009), The Benguela Current: An ecosystem of four
 571 components, *Prog. Oceanogr.*, *83*, 15-32, doi:10.1016/j.pocean.2009.07.046
 572 Johnson, G. C. (2001), The Pacific Ocean subtropical cell surface limb. *Geophys. Res.*
 573 *Lett.*, *28*, 1771-1774, doi:10.1029/2000GL012723.
 574 Johnson, G. C., M. J. McPhaden, and E. Firing (2001), Equatorial Pacific Ocean
 575 horizontal velocity, divergence, and upwelling. *J. Phys. Oceanogr.*, **31**, 839–849,
 576 doi:10.1175/1520-0485(2001)031<0839:EPOHVD>2.0.CO;2.
 577 Johnson, G. C., M. J. McPhaden, G. D. Rowe, and K. E. McTaggart (2000). Upper
 578 equatorial Pacific Ocean current and salinity variability during the 1996–1998 El
 579 Niño–La Niña cycle. *J. Geophys. Res.*, *105*, 1037–1053, doi:10.1029/1999JC900280.
 580 Johnson, G. C., B. M. Sloyan, W. S. Kessler, and K. E. McTaggart (2002), Direct
 581 measurements of upper ocean currents and water properties across the tropical Pacific
 582 Ocean during the 1990's, *Progress in Oceanography*, *52*, 31–61, doi:10.1016/S0079-
 583 6611(02)00021-6.
 584 Kelly, K. A., S. Dickinson, M. J. McPhaden, and G. C. Johnson (2001), Ocean currents
 585 evident in satellite wind data, *Geophysical Research Letters*, *28*, 2469–2472,
 586 doi:10.1029/2000GL012610.
 587 Law, K. L., S. Morét-Ferguson, N. A. Maximenko, G. Proskurowski, E. E. Peacock, J.
 588 Hafner, and C. M. Reddy (2010), Plastic Accumulation in the North Atlantic
 589 Subtropical Gyre, *Science*, *329*, 1185–1188, doi:10.1126/science.1192321.
 590 Lumpkin, R. (2003), Decomposition of surface drifter observations in the Atlantic

591 Ocean, *Geophys. Res. Lett.*, 30 (14), 1753, doi:10.1029/2003GL017519.
 592 Lumpkin, R. and S. Garzoli (2005), Near-surface circulation in the Tropical Atlantic
 593 Ocean, *Deep-Sea Res. I*, 52, 495–518.
 594 Lumpkin, R., and M. Pazos (2007), Measuring surface currents with Surface Velocity
 595 Program drifters: the instrument, its data and some recent results, in *Lagrangian*
 596 *Analysis and Prediction of Coastal and Ocean Dynamics*, edited by A. Griffa, A. D.
 597 Kirwan, A. Mariano, T. Özgökmen, and T. Rossby, chap. 2, pp. 39–67, Cambridge
 598 University Press.
 599 Lumpkin, R. and S. L. Garzoli (2011), Interannual to Decadal Variability in the
 600 Southwestern Atlantic’s Surface Circulation, *J. Geophys. Res.-Oceans*, 116, C01014,
 601 doi:10.1029/2010JC006285.
 602 Lumpkin, R., S. Grodsky, L. Centurioni, M.-H. Rio, J. Carton and D. Lee (2012),
 603 Removing spurious low-frequency variability in drifter velocities, *J. Atmos. Oceanic*
 604 *Technol.*, in revision [minor revisions necessary].
 605 Lutjeharms, J. R. E. (2007). Three decades of research on the greater Agulhas Current,
 606 *Ocean Sci.*, 3, 129–147, doi:10.5194/os-3-129-2007.
 607 Maximenko, N., P. Niiler, M.-H. Rio, O. Melnichenko, L. Centurioni, D. Chambers, V.
 608 Zlotnicki, and B. Galperin (2009), Mean dynamic topography of the ocean derived
 609 from satellite and drifting buoy data using three different techniques, *J. Atmos.*
 610 *Oceanic Technol.*, 26, 1910–1919, doi:10.1175/2009JTECHO672.1
 611 Maximenko, N., J. Hafner, and P. Niiler (2012), Pathways of marine debris derived from
 612 trajectories of Lagrangian drifters, *Mar. Pollut. Bull.*, 65, 51–62,
 613 doi:10.1016/j.marpolbul.2011.04.016.

614 McCord, M. R., Y. K. Lee, and H. K. Lo (1999), Ship routing through altimetry-derived
615 ocean currents, *Transport. Sci.*, 33, 49–67, doi:10.1287/trsc.33.1.49.

616 Nagura, M., and M. J. McPhaden (2010), Wyrтки Jet dynamics: Seasonal variability, *J.*
617 *Geophys. Res.*, 115, C07009, doi:10.1029/2009JC005922.

618 Niiler, P. P. (2001), The world ocean surface circulation, in *Ocean Circulation and*
619 *Climate*, International Geophysics Series, 77, edited by G. Siedler, J. Church, and J.
620 Gould, pp. 193–204, Academic Press.

621 Niiler, P. P., A. Sybrandy, K. Bi, P. Poulain, and D. Bitterman (1995), Measurements of
622 the water-following capability of holey-sock and TRISTAR drifters, *Deep Sea Res.*,
623 42, 1951–1964.

624 Niiler, P. P. and J. D. Paduan (1995), Wind-driven motions in the northeast Pacific as
625 measured by Lagrangian drifters, *J. Phys. Oceanogr.* 25, 2819-2830.

626 Nykjær, L., and L. Van Camp (1994), Seasonal and interannual variability of coastal
627 upwelling along northwest Africa and Portugal from 1981 to 1991, *J. Geophys. Res.*,
628 99, 14,197–14,207, doi:10.1029/94JC00814.

629 Orsi, A. H., T. Whitworth III and W. D. Nowlin, Jr., (1995), On the meridional extent
630 and fronts of the Antarctic Circumpolar Current, *Deep-Sea Res. I*, 42, 641–
631 673. Palacios, D. M. and S. J. Bograd (2005), A census of Tehuantepec and Papagayo
632 eddies in the northeastern tropical Pacific, *Geophys. Res. Lett.*, 32, 23606, doi:
633 10.1029/2005GL024324.

634 Pazan, S. E., and P. P. Niiler (2001), Recovery of near-surface velocity from undrogued
635 drifters, *J. Atmos. Oceanic Technol.*, 18, 476–489.

636 Perez, R. C., M. F. Cronin and W. S. Kessler (2010), Tropical Cells and a Secondary

637 Circulation near the Northern Front of the Equatorial Pacific Cold Tongue, *J. Phys.*
638 *Oceanogr.*, *40*, 2091–2106.

639 Potemra, J. T., and N. Schneider (2007), Interannual variations of the Indonesian
640 throughflow, *J. Geophys. Res.*, *112*, C05035, doi:10.1029/2006JC003808.

641 Poulain, P.-M., R. Gerin, E. Mauri, and R. Pennel (2009), Wind effects on drogued and
642 undrogued drifters in the eastern Mediterranean, *J. Atmos. Oceanic Technol.*, *26*,
643 1144–1156, doi:10.1175/2008JTECHO618.1.

644 Poulain, P.-M., A. Warn-Varnas, and P. P. Niiler (1996), Near-surface circulation of the
645 Nordic seas as measured by Lagrangian drifters, *J. Geophys. Res.*, *101*, 18,237–
646 18,258, doi:10.1029/96JC00506.

647 Provost, C., O. Garcia, and V. Garçon (1992), Analysis of satellite sea surface
648 temperature time series in the Brazil-Malvinas Current confluence region: Dominance
649 of the annual and semiannual periods, *J. Geophys. Res.*, *97*, 17,841–17,858,
650 doi:10.1029/92JC01693.

651 Qu, T., H. Mitsudera, and B. Qiu (2001), A climatological view of the Kuroshio/Oyashio
652 system east of Japan, *J. Phys. Oceanogr.*, *31*, 2575–2589, doi:10.1175/1520-
653 0485(2001)031<2575:ACVOTK>2.0.CO;2.

654 Qu, T., H. Mitsudera, and T. Yamagata (1999), A Climatology of the Circulation and
655 Water Mass Distribution near the Philippine Coast, *J. Phys. Oceanogr.*, *29*, 1488–
656 1505.

657 Reed, R.K. (1984), Flow of the Alaskan Stream and its variations, *Deep-Sea Res.*, *31*,
658 369–386, doi:10.1016/0198-0149(84)90090-6.

659 Richardson, P. L. (2005), Caribbean Current and eddies as observed by surface drifters,

660 *Deep-Sea Res.*, 52, 429–463, doi:10.1016/j.dsr2.2004.11.001.

661 Rio, M. H., S. Guinehut, and G. Larnicol (2011), New CNES-CLS09 global mean
 662 dynamic topography computed from the combination of GRACE data, altimetry and
 663 in situ measurements, *J. Geophys. Res.*, 116, C07,018, doi:10.1029/2010JCOO6505.

664 Risien, C. M., and D. B. Chelton (2008), A global climatology of surface wind and wind
 665 stress fields from eight years of QuikSCAT scatterometer data, *J. Phys. Oceanogr.*,
 666 38, 2379–2413, doi: 10.1175/2008JPO3881.1.

667 Schmitz, W. J., Jr., and M. S. McCartney (1993), On the North Atlantic Circulation, *Rev.*
 668 *Geophys.*, 31, 29–49, doi:10.1029/92RG02583.

669 Schott, F. A., and J. P. McCreary, Jr. (2001), The monsoon circulation of the Indian
 670 Ocean, *Prog. Oceanogr.*, 51, 1–123.

671 Schott, F. A., J. P. McCreary, Jr., and G. C. Johnson (2004), Shallow overturning
 672 circulations of the tropical-subtropical oceans, in *Earth Climate: The Ocean-*
 673 *Atmosphere Interaction*, C. Wang, S.-P. Xie, and J. A. Carton, Eds., American
 674 Geophysical Union Geophysical Monograph 147, 261–304.

675 Schott, F., J. C. Swallow, and M. Fieux (1990), The Somali current at the equator: annual
 676 cycle of currents and transports in the upper 1000 m and connection to neighbouring
 677 latitudes, *Deep-Sea Res. A*, 37, 1825–1848, doi:10.1016/0198-0149(90)90080-F.

678 Sloyan, B. M., and S. R. Rintoul (2001). The Southern Ocean limb of the global deep
 679 overturning circulation, *J. Phys. Oceanogr.*, 31, 143–173, doi:10.1175/1520-
 680 0485(2001)031<0143:TSOLOT>2.0.CO;2.

681 Stammer, D. (1997), Global characteristics of ocean variability estimated from regional
 682 TOPEX/POSEIDON altimeter measurements, *J. Phys. Oceanogr.*, 27, 1743–1769.
 683 doi:10.1175/1520-0485(1997)027<1743:GCOOVE>2.0.CO;2
 684 Swallow, J., M. Fieux, and F. Schott (1988), The Boundary Currents East and North of
 685 Madagascar 1. Geostrophic Currents and Transports, *J. Geophys. Res.*, 93, 4951–
 686 4962, doi:10.1029/JC093iC05p04951.
 687 Toole, J. M., R. C. Millard, Z. Wang, and S. Pu (1990), Observations of the Pacific North
 688 Equatorial Current bifurcation at the Philippine coast, *J. Phys. Oceanogr.*, 20, 307–
 689 318, doi:10.1175/1520-0485(1990)020<0307:OOTPNE>2.0.CO;2.
 690 Trenberth, K. E. (1984), Signal versus noise in the Southern Oscillation, *Mon. Weath.*
 691 *Rev.*, 112, 326–332.
 692 Wunsch, C. (1996), *The Ocean Circulation Inverse Problem*, Cambridge University
 693 Press, New York.
 694 Wunsch, C. (1998), The Work Done by the Wind on the Oceanic General Circulation, *J.*
 695 *Phys. Oceanogr.*, 28, 2332–2340.
 696 Yoder, J. A., S. G. Ackleson, R. T. Barber, P. Flament, and W. M. Balch (1994), A line
 697 in the sea, *Nature*, 371, 689–692, doi:10.1038/371689a0.
 698

Figure Captions

Figure 1. Number of drogued drifter observations used to map fields at each grid point bin (in drifter days per square degree).

Figure 2. Mean current speeds (colors, in cm s^{-1}) from near-surface surface drifter data with streamlines (black lines). Streamlines are calculated from spatially smoothed currents to indicate flow direction and qualitatively illustrate large-scale circulation features, including surface divergence. Light gray areas have less than 12 drifter days per square degree. In addition, only bins with mean current speeds statistically different from zero at one standard error of the mean are shaded.

Figure 3. Variance ellipses centered every 5° longitude by 2° latitude (black lines) over the square root of the magnitude of variance (colors in cm s^{-1}). Light gray areas have less than 12 drifter days per square degree.

Figure 4. Speed of currents regressed onto the Southern Oscillation Index (colors in cm s^{-1}) shown for $\text{SOI} = -1$ (moderate El Niño) with directions (black arrows) indicated at for a subset of gridpoints. Gridpoints with values that are not significantly different from zero at one standard error of the mean not displayed.

Figure 5. Near-surface ocean currents from surface drifter data. Details follow Fig. 2, except displayed for climatological February (top panel) and August (bottom panel).

721

722 Figure 6. Near-surface ocean currents from surface drifter data. Details follow Fig. 2,
723 except displayed for climatological May (top panel) and November (bottom panel).

724

725 Figure 7. Seasonal variations of surface currents (black arrows, see key in lower left
726 panel) in the northwestern tropical Pacific Ocean. Currents are not shown where they are
727 not significantly different from zero at one standard error of the mean.

728

729 Figure 8. Seasonal cycle of surface divergence (colors, 10^{-8} s^{-1}) vs. latitude averaged over
730 longitude bands in the interior of the a) Indian ($90^{\circ}\text{E} - 55^{\circ}\text{E}$), b) Pacific ($165^{\circ}\text{E} - 85^{\circ}\text{W}$),
731 and c) Atlantic ($30^{\circ}\text{W} - 5^{\circ}\text{E}$) Oceans. Tick marks show the start of named months.

732

733 Figure 9. Fractions (colors, upper colorbar) of (a) time mean, (b), eddy, and (c) seasonal
734 contributions to the total surface kinetic energy in the drifter climatology along with (d)
735 the total kinetic energy (colors, $\text{m}^2 \text{ s}^{-2}$, lower colorbar).

736

737 Figure 10. Vector differences (arrows; colors indicate difference magnitudes in cm s^{-1}),
738 time-mean velocity of drifters minus a) January 1993–December 2003 time-mean total
739 speed from NOAA’s 1/3 degree unsmoothed Ocean Surface Current Analysis Real-time
740 (OSCAR) product [Bonjean and Lagerloef, 2002] including geostrophic, Ekman and
741 buoyancy components, and b) time-mean geostrophic speed from the CNES-CLS 2009
742 v1.1 Mean Dynamic Topography [Rio et al., 2011].

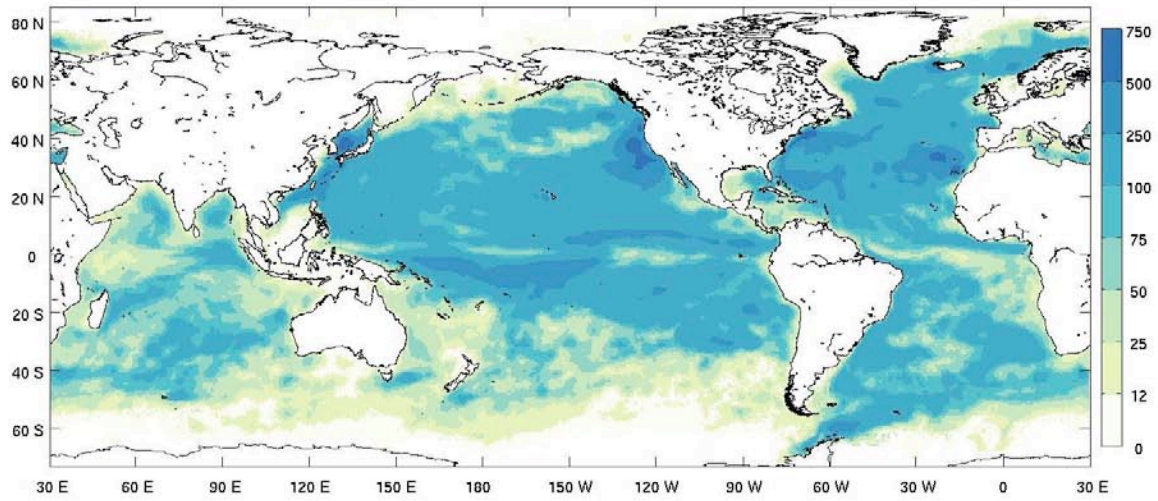


Figure 1. Number of drogued drifter observations used to map fields at each grid point bin (in drifter days per square degree).

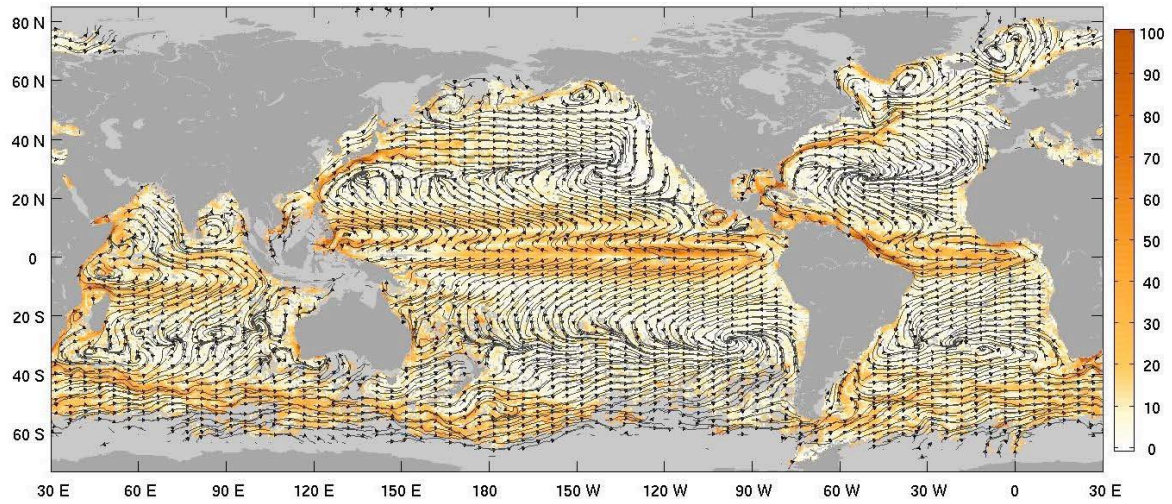


Figure 2. Mean current speeds (colors, in cm s^{-1}) from near-surface surface drifter data with streamlines (black lines). Streamlines are calculated from spatially smoothed currents to indicate flow direction and qualitatively illustrate large-scale circulation features, including surface divergence. Light gray areas have less than 12 drifter days per square degree. In addition, only bins with mean current speeds statistically different from zero at one standard error of the mean are shaded.

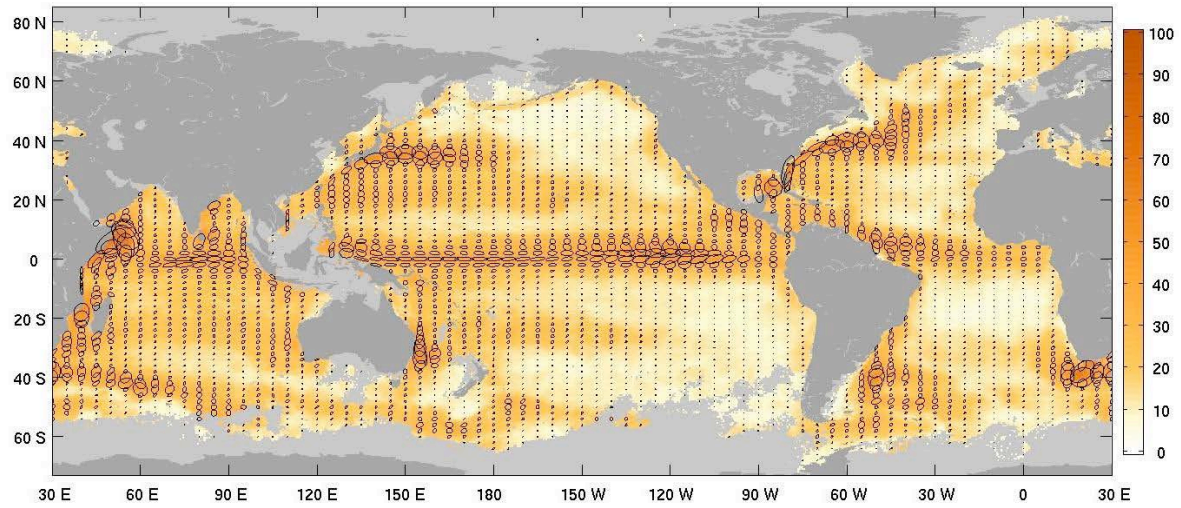


Figure 3. Variance ellipses centered every 5° longitude by 2° latitude (black lines) over the square root of the magnitude of variance (colors in cm s^{-1}). Light gray areas have less than 12 drifter days per square degree.

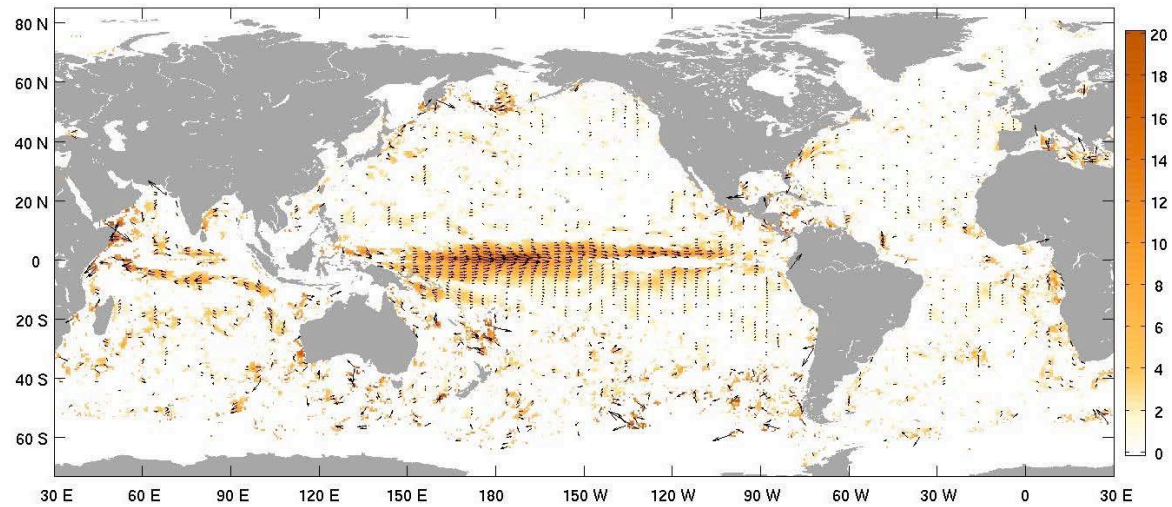


Figure 4. Speed of currents regressed onto the Southern Oscillation Index (colors in cm s^{-1}) shown for $\text{SOI} = -1$ (moderate El Niño) with directions (black arrows) indicated at for a subset of gridpoints. Gridpoints with values that are not significantly different from zero at one standard error of the mean not displayed.

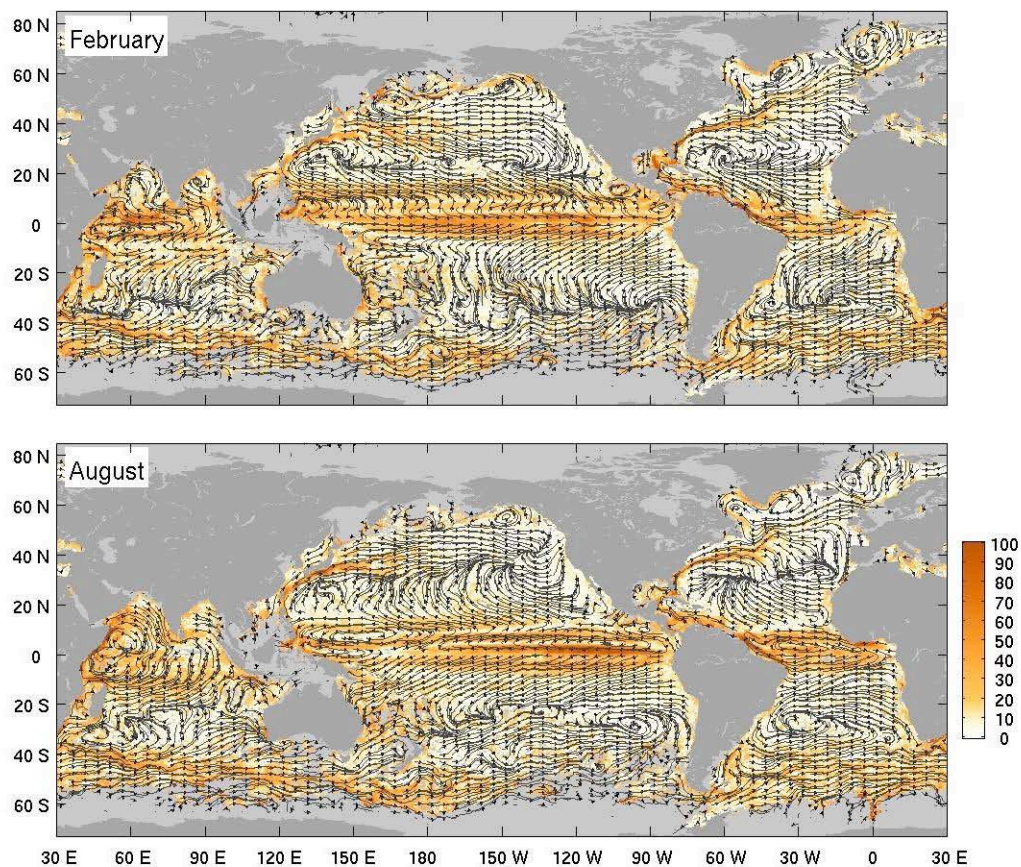


Figure 5. Near-surface ocean currents from surface drifter data. Details follow Fig. 2, except displayed for climatological February (top panel) and August (bottom panel).

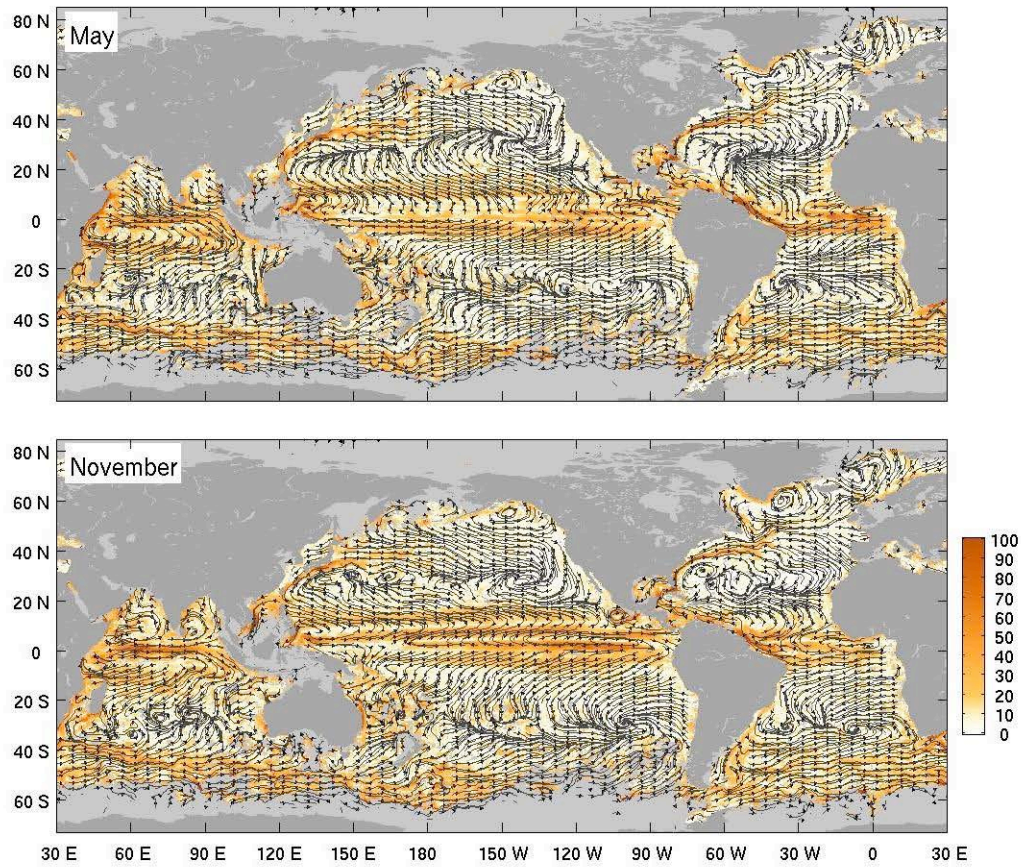


Figure 6. Near-surface ocean currents from surface drifter data. Details follow Fig. 2, except displayed for climatological May (top panel) and November (bottom panel).

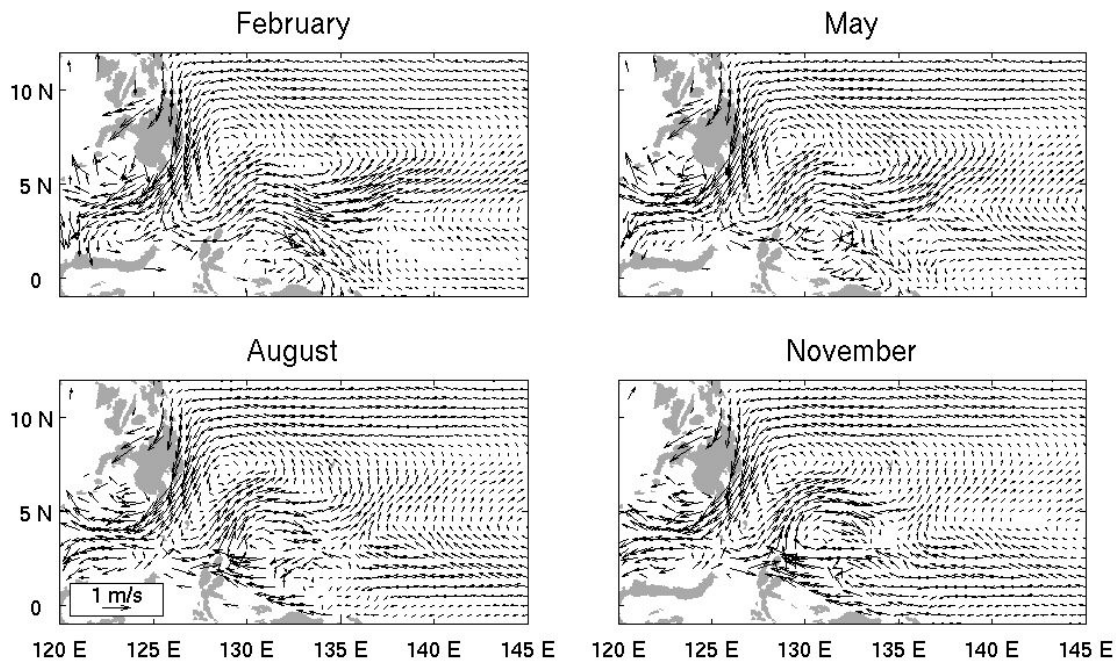


Figure 7. Seasonal variations of surface currents (black arrows, see key in lower left panel) in the northwestern tropical Pacific Ocean. Currents are not shown where they are not significantly different from zero at one standard error of the mean.

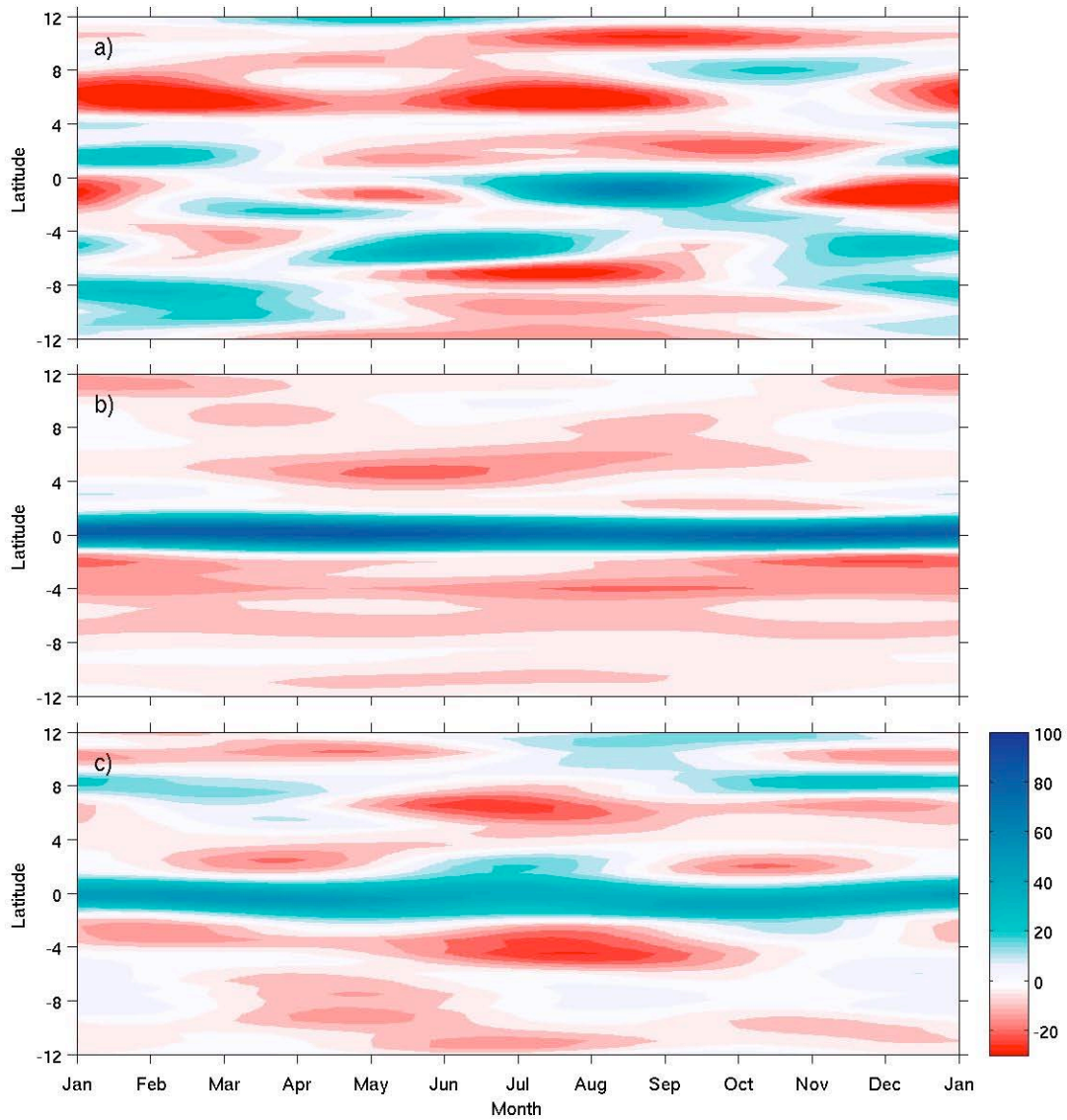


Figure 8. Seasonal cycle of surface divergence (colors, 10^{-8} s^{-1}) vs. latitude averaged over longitude bands in the interior of the a) Indian ($90^{\circ}\text{E} - 55^{\circ}\text{E}$), b) Pacific ($165^{\circ}\text{E} - 85^{\circ}\text{W}$), and c) Atlantic ($30^{\circ}\text{W} - 5^{\circ}\text{E}$) Oceans. Tick marks show the start of named months.

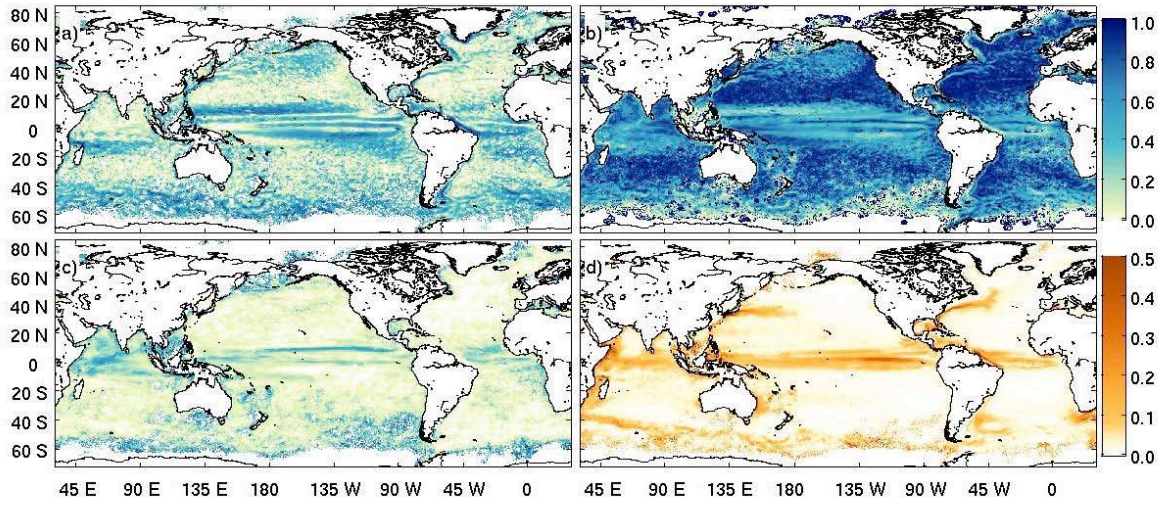


Figure 9. Fractions (colors, upper colorbar) of (a) time mean, (b), eddy, and (c) seasonal contributions to the total surface kinetic energy in the drifter climatology along with (d) the total kinetic energy (colors, $\text{m}^2 \text{s}^{-2}$, lower colorbar).

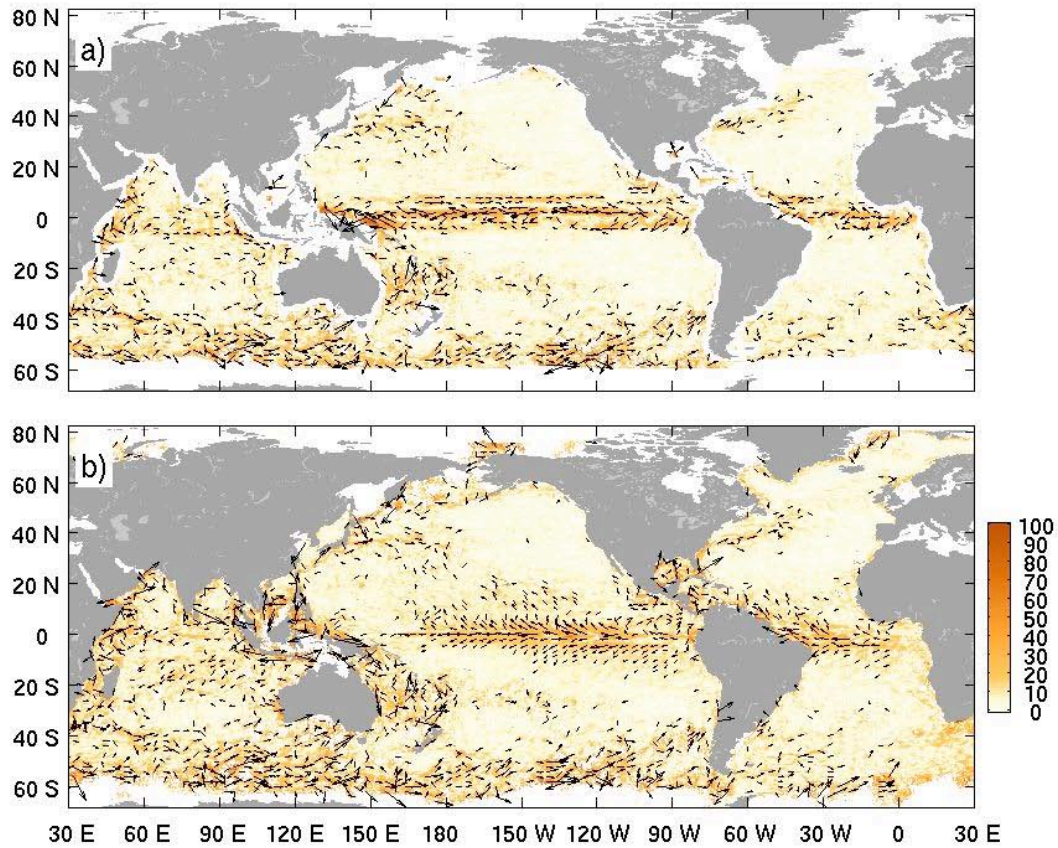


Figure 10. Vector differences (arrows; colors indicate difference magnitudes in cm s^{-1}), time-mean velocity of drifters minus a) January 1993–December 2003 time-mean total speed from NOAA's 1/3 degree unsmoothed Ocean Surface Current Analysis Real-time (OSCAR) product [Bonjean and Lagerloef, 2002] including geostrophic, Ekman and buoyancy components, and b) time-mean geostrophic speed from the CNES-CLS 2009 v1.1 Mean Dynamic Topography [Rio *et al.*, 2011].